Research Square

Preprints are preliminary reports that have not undergone peer review.
They should not be considered conclusive, used to inform clinical practice,
or referenced by the media as validated information.

Heterogeneous synthesis of perovskite quantum dots for efficient blue LEDs

Guogang Li

ggli@cug.edu.cn

China University of Geosciences https://orcid.org/0000-0002-0523-5621

Jie Chen

China University of Geosciences

Wanying Zhang

Wuhan University of Technology

Xinyang Zhang

China University of Geosciences

Yingwei Wang

Central South University https://orcid.org/0000-0003-1828-8420

Zhuoyin Peng

Changsha University of Science & Technology

Fan Xia

State Key Laboratory of Geomicrobiology and Environmental Changes, Faculty of Materials Science and Chemistry, China University of Geosciences https://orcid.org/0000-0001-7705-4638

Keqiang Chen

China University of Geosciences https://orcid.org/0000-0002-5741-1236

Article

Keywords:

Posted Date: November 20th, 2026

DOI: https://doi.org/10.21203/rs.3.rs-11778511/v1

License: This work is licensed under a Creative Commons Attribution 4.0 International License.
Read Full License

Additional Declarations: There is **NO** Competing Interest.

Abstract

The controllable synthesis of high-quality quantum dots (QDs) has long been governed by a strict paradigm requiring fully dissolved precursors to ensure homogeneous nucleation. Conversely, heterogeneous conditions with undissolved solid precursors are universally regarded as a “forbidden zone” because they trigger uncontrolled nucleation, yielding broad size distributions and irregular morphologies. Here, we overturn this long-standing paradigm by demonstrating a heterogeneous synthesis strategy for high-performance blue-emitting perovskite QDs. By exploiting their sub-second nucleation and growth kinetics, we intentionally retain solid lead halide grains as a highly dynamic precursor reservoir. This reservoir acts as a thermodynamic buffer that continuously modulates the monomer supply, thereby introducing precursor phase behavior as an entirely new dimension to simultaneously lower the interior chloride content and construct an ordered, chloride-rich surface. The resulting quasi-core-shell structure effectively suppresses deep-level defects and substantially enhances exciton localization. Consequently, the blue perovskite QD-based light-emitting diodes (LEDs) achieve a record external quantum efficiency (EQE) of 37.56% at 476 nm (with a third-party certified EQE of 36.96%), alongside record efficiencies across the entire blue spectrum from deep-blue to cyan. This work establishes a generalizable paradigm for manipulating QD growth thermodynamics and defect chemistry in next-generation optoelectronic devices.

Introduction

Colloidal quantum dots (QDs) have been widely explored for optoelectronic applications owing to their tunable physicochemical properties[1,2]. Over the past three decades, their synthesis methods have become increasingly diverse[3,4]. The LaMer model is commonly used to describe the nucleation and growth process of QDs[5]. In conventional QDs (e.g., II–VI and III–V QDs), this model allows clear temporal separation of nucleation and growth through careful synthetic engineering[6]. Crucially, achieving high-quality QDs demands a homogeneous initial state, with all precursors fully dissolved and uniformly mixed, so that the degree of supersaturation is identical at every point when nucleation is triggered[7]. In a heterogeneous system containing undissolved solid precursors, these solids become preferential nucleation centers, causing heterogeneous nucleation and direct growth on their surfaces[8]. The resulting inability to decouple nucleation from growth yields products with broad size dispersion, polycrystallinity or irregular morphology[9].

For perovskite QDs, however, the nucleation and growth kinetics occur on a sub-second timescale, meaning that nucleation and growth are not temporally separated[10,11]. During synthesis, each nucleus grows essentially independently, and the process is too fast to allow Ostwald ripening, which would otherwise broaden the size distribution[12,13]. Theoretically, this independent, rapid growth may render the system largely insensitive to the presence of undissolved precursor solids. Even if such solids provide heterogeneous nucleation sites, they should have negligible influence on the growth of the other nuclei. Subsequent centrifugal purification can easily isolate the high-quality perovskite QDs formed in the bulk

solution. Thus, the ultra-fast, temporally overlapped kinetics of perovskite QDs relax the traditional requirement for perfect precursor homogeneity and open a possible pathway toward heterogeneous synthesis.

Here, by exploiting this pathway, we developed a heterogeneous synthesis strategy in which solid lead halide grains remain undissolved, aiming to overcome the critical limitation of blue perovskite QDs that the high chloride content required for wide-bandgap emission introduces deep-level defects and instability[14–17]. These undissolved solid grains act as a dynamic precursor reservoir and thermodynamic buffer, continuously modulating the monomer supply, thereby simultaneously reducing the Cl content in the final mixed-halide QDs, suppressing Cl-vacancy-induced deep-level defects, and enabling in situ surface passivation. The resulting $CsPbBr_xCl_{3-x}$ blue QDs feature a Cl-poor interior and an ordered, Cl-rich surface, forming a quasi-core-shell structure with substantially enhanced optical properties across the entire 447–487 nm range. The corresponding blue light-emitting diodes (LEDs) achieve a record-breaking EQE of 37.56% at 476 nm, and by fine-tuning the Cl/Br stoichiometry, we also reach record values at 453 nm (6.13%), 463 nm (25.50%), 473 nm (36.39%) and 483 nm (35.48%). More broadly, this work establishes a generalizable paradigm for manipulating QD growth thermodynamics through precursor phase behavior, offering a broadly applicable route for defect engineering and performance enhancement in high-performance QD-based optoelectronic devices.

Results and discussion

Formation thermodynamics modulation

We devised a heterogeneous synthesis of mixed-halide $CsPbBr_xCl_{3-x}$ QDs based on a modified ligand-assisted reprecipitation method (see Methods for details), as illustrated in Fig. 1a and Supplementary Fig. 1[18]. This process comprises three stages: dissolution of lead halides (PbX_2, including $PbCl_2$ and $PbBr_2$), QD formation, and surface passivation. In the first stage, tetra-*n*-octylammonium bromide (TOAB) acts as the primary dissolution agent, with a clear preference for $PbBr_2$ (Supplementary Fig. 2). In the homogeneous case, excess TOAB completely dissolves PbX_2, making the Cl/Br ratio identical to the feed ratio. In contrast, our heterogeneous approach uses excess PbX_2 with a limited amount of TOAB, producing a solid-liquid two-phase mixture consisting of a saturated $TOA^+[PbX_n]^-$ solution and solid PbX_2 precipitate. The insufficient TOAB forces competitive dissolution of $PbCl_2$ and $PbBr_2$, while the preferential dissolution of $PbBr_2$ lowers the Cl/Br ratio below the feed ratio (Fig. 1b and Supplementary Fig. 3). Subsequent addition of dodecylbenzenesulfonic acid (DBSA) generates less reactive, incompletely ionized hydrogen halides (HX) and PbX_2[19]. The higher electronegativity of chlorine (3.16) compared with bromine (2.96) promotes the preferential formation of HCl and $PbCl_2$[20]. In the heterogeneous system, the competitive dissolution of $PbCl_2$ and $PbBr_2$ further amplifies this effect, leading to more effective depletion of Cl^-. This cascade further reduces the Cl/Br ratio and consequently the Cl content in the final QDs, an effective means of suppressing Cl vacancy induced deep-level defects.

Upon injection of the Cs precursor, Cs^+ reacts with $TOA^+[PbX_n]^-$ to form $CsPbBr_xCl_{3-x}$ QDs, releasing bulky TOA^+ cation with large steric hindrance into the solution[21,22]. In the homogeneous route, this TOA^+ is inert. By contrast, in the heterogeneous system, the released TOA^+ ions react with the solid PbX_2 precipitate to regenerate $TOA^+[PbX_n]^-$ in situ, thereby driving the formation equilibrium forward to supply fresh monomers. In this way, the solid PbX_2 grains act as a dynamic reservoir and thermodynamic buffer that continuously regulates monomer availability. Given the sub-second nucleation and growth kinetics of $CsPbBr_xCl_{3-x}$ QDs, this slow monomer release does not trigger new nucleation, instead, it supplies precursors that predominantly passivate surface defects. This is evidenced by the time-dependent increase in photoluminescence (PL) lifetime and PL quantum yield (PLQY) of QDs synthesized by heterogeneous approach (hetero-QDs), while QDs synthesized by homogeneous route (homo-QDs) remain nearly constant (Fig. 1c). Control experiments by removing PbX_2 precipitate prior to Cs injection show no such improvement (Supplementary Fig. 4), directly confirming the essential role of solid PbX_2 precipitate in tuning the reaction thermodynamics. We also monitored the PL peak during the reaction (Supplementary Figs. 5a,b). Homo-QDs maintain an almost fixed emission peak, while hetero-QDs undergo a clear red shift (480 → 488 nm). We attribute this red shift to preferential re-dissolution of $PbBr_2$, which further reduces the Cl content. These results demonstrate that the solid PbX_2 precipitate not only modulates the growth thermodynamics to enable in situ passivation, but also suppresses deep-level defects by further reducing the Cl content, underscoring the superiority of the heterogeneous strategy.

In the final passivation stage, a small amount of didodecyldimethylammonium chloride (DDAC) is added. In the case of homo-QDs, the high concentration of residual Cl^- in the reaction system minimizes the influence of subsequently added DDAC on the equilibrium, leading to only a slight blue shift (479 → 478 nm, Fig. 1d and Supplementary Fig. 5c). By contrast, in the heterogeneous system, the low concentration of active Cl^- drives a substantial shift in the reaction equilibrium towards perovskite formation, giving rise to a pronounced blue shift (488 → 482 nm, Fig. 1d and Supplementary Fig. 5d). Moreover, because the Cl content in hetero-QDs is significantly reduced, we infer that the Cl^- supplied by DDAC enriches the QD surface relative to the core, forming a Cl-rich surface layer akin to a $CsPbBr_xCl_{3-x}/CsPbCl_3$ quasi-core-shell structure.

To verify this hypothesis, we analyzed the halogen distribution in the $CsPbBr_xCl_{3-x}$ QDs using in situ X-ray photoelectron spectroscopy (XPS) depth profiling, with the etching depth set to 8 nm based on the QD size (Supplementary Figs. 6–7). The homo-QDs possess an inhomogeneous Cl distribution with a distinctly Cl-poor region (Fig. 2a and Supplementary Fig. 8), implying abundant chlorine vacancies. In contrast, hetero-QDs possess a lower overall Cl content but a uniform distribution and, crucially, a slightly higher Cl concentration at the surface than in the interior, verifying the quasi-core-shell structure. Colloidal ^{133}Cs nuclear magnetic resonance (NMR) spectroscopy reveals an up-field shift for hetero-QDs (88.01 ppm vs. 91.74 ppm for homo-QDs, Fig. 2b) consistent with a smaller size. Normally, size reduction broadens the signal owing to increased surface disorder, yet the full width at half-maximum

(FWHM) of hetero-QDs is narrower (Fig. 2b), indicating a more ordered surface[23]. This improved structural order, in line with the XPS results, is highly beneficial for reducing trap state density and enhancing optoelectronic properties.

Optoelectronic properties characterization

We characterized the electrical properties of the as-prepared $CsPbBr_xCl_{3-x}$ QDs by Kelvin probe force microscopy (KPFM) and conductive atomic force microscopy (C-AFM). The KPFM contact potential difference (CPD) maps in Figs. 2c,d reveal that the film based on hetero-QDs exhibits a more uniform surface potential than the homo-QD film, consistent with a lower defect density in the former[24]. C-AFM measurements show that the hetero-QD film sustains markedly higher local currents (Supplementary Fig. 9). Given that both types of QDs share identical surface ligands, this conductivity enhancement can be attributed to the reduced defect density. Femtosecond transient absorption (TA) spectroscopy provides further insight into the excited-state dynamics. The ground-state bleach (GSB) linewidth of homo-QDs is markedly broader than that of hetero-QDs (Figs. 2e,f), revealing substantial spectral heterogeneity. Specifically, the homo-QD film exhibits two distinct bleach features centered at 475 and 483 nm, corresponding to the original component and a Br-rich phase, respectively (Supplementary Fig. 10)[25]. This Br-rich phase, driven by Cl vacancies and halide-ion segregation, is substantially suppressed in the hetero-QDs, underscoring the crucial role of the heterogeneous synthesis in inhibiting defect-mediated phase separation and maintaining compositional homogeneity.

Benefiting from the optimized surface and reduced defect density, hetero-QDs demonstrate superior environmental and thermal stability to homo-QDs, as shown in Supplementary Figs. 11–12. Moreover, the hetero-QDs exhibit a higher exciton binding energy (E_b) than their homo-counterparts (Supplementary Fig. 13), which facilitates radiative recombination and improves LED performance. Encouraged by these improvements, we thus extended the heterogeneous approach to the entire blue region, synthesizing QDs with PL peaks from 447 to 487 nm that span deep-blue, pure-blue, sky-blue, and cyan (Fig. 2g and Supplementary Tables 1–2). These QDs show consistently higher PLQYs than the homo-QDs (Fig. 2h). Subsequent introduction of tetraoctylammonium fluoride (TOAF), which can passivate the surface halogen vacancy defects, further boosted the PLQY to > 95% for the 478–487 nm range (hetero-TOAF-QDs, Supplementary Figs. 14–18).

High-efficiency blue LEDs

We then fabricated LEDs using the three types of QDs with the architecture of indium tin oxide (ITO)/poly(ethylenedioxythiophene):poly(styrenesulfonate) (PEDOT:PSS)/nafion perfluorinated ionomer (PFI)/poly(9,9-n-diphenyl-2,7-fluorene-alt-9-isophenyl-3,6-carbazole) (PF8Cz)/QDs/1,3,5-tris(1-phenyl-1H-benzimidazol-2-yl)benzene (TPBi)/2,4,6-tris[3-(diphenylphosphino)phenyl]-1,3,5-triazole (PO-T2T)/lithium fluoride (LiF)/Al (Fig. 3a and Supplementary Fig. 19). All these devices show sky-blue emission, and the electroluminescence (EL) intensity increases progressively from homo-, hetero-, to hetero-TOAF- QD-

based LEDs (Figs. 3b,c and Supplementary Fig. 20). At an identical driving voltage of 6 V, the current densities of hetero- and hetero-TOAF devices surpass that of the homo-device by factors of 1.3 and 2.5 (Fig. 3d). Correspondingly, they achieve peak luminance of 1,326 and 3,029 cd m^{-2}, 4.2- and 9.6-fold higher than the homo-device value (315 cd m^{-2}, Fig. 3e). These gains translate into a marked increase in EQE, from 14.75% (homo) to 26.12% (hetero) and 37.56% (hetero-TOAF, third-party certified EQE of 36.96%), as shown in Fig. 3f and Supplementary Fig. 21. To the best of our knowledge, the latter represents the highest EQE reported for blue perovskite LEDs. The hetero- and hetero-TOAF devices also exhibit substantially improved operational stability (Supplementary Fig. 22) and significantly higher EQEs at peak luminance (4.18% and 4.76%, respectively) compared with the homo-device (0.33%, Fig. 3g). Statistical analysis of 25 devices confirms excellent reproducibility, with average EQEs rising from 11.88% (homo) to 23.97% (hetero) and 34.76% (hetero-TOAF) (Fig. 3h).

To understand the origin of these improvements, we measured the film conductivity using an ITO/QDs/Al structure. The hetero- and hetero-TOAF- QD films show 1.57- and 1.77-fold higher conductivity than the homo-QD film, facilitating carrier transport and supporting the observed higher current densities (Fig. 3i)[24]. Transient photocurrent measurements further reveal that both hetero- and hetero-TOAF LEDs exhibit nearly vertical current rise and fall edges, whereas the homo-LED displays pronounced current overshoot during voltage switching (Supplementary Fig. 23). The negligible overshoot and rapid stabilization in the hetero-based devices indicate a reduced density of interfacial traps and suppressed charge trapping/detrapping processes[26,27]. We also examined ion migration in the three QD films. The derived activation energies (E_a) are 336, 496, and 531 meV for homo-, hetero-, and hetero-TOAF- QDs, respectively (Supplementary Fig. 24)[28]. The higher E_a mitigates ion-migration-induced degradation, contributing to the enhanced stability. Direct optical microscopy observation under a constant electric field of 2.0 V μm^{-1} for 4 hours reveals extensive dark regions in the homo-QD film, indicative of destructive degradation including phase segregation and octahedral decomposition driven by ion migration, whereas the hetero- and hetero-TOAF- based films show obviously mitigated degradation (Supplementary Fig. 25). Consistently, the hetero- and hetero-TOAF devices show significantly suppressed current-voltage hysteresis (Supplementary Fig. 26), further evidencing restrained ion migration[29]. Collectively, these results demonstrate that hetero- and hetero-TOAF- QDs possess higher conductivity, fewer interfacial traps, and suppressed ion migration, providing a solid foundation for their high EQE and improved stability.

To decouple the contributions of TOAF passivation and the heterogeneous synthesis itself, we fabricated additional control devices using TOAF-modified homo-QDs (homo-TOAF), QDs synthesized without PbX_2 precipitate (hetero w/o precipitate), and the same precipitate-free QDs further passivated by TOAF (hetero w/o precipitate TOAF). These devices exhibit peak EQEs of 19.28%, 18.95%, and 20.51%, respectively (Supplementary Fig. 27). Together with the results above, these data confirm that while TOAF passivation is an effective defect-healing strategy, the thermodynamic modulation achieved by the heterogeneous synthesis plays the more decisive role in boosting EQE.

We then extended this high-performance platform to the entire blue spectral region by employing hetero-TOAF QDs with different emission wavelengths as the emissive layer. Representative devices with deep-blue (453 nm), pure-blue (463 nm), sky-blue (473 nm), and cyan (483 nm) EL peaks achieve peak EQEs of 6.13%, 25.67%, 36.40%, and 35.49%, respectively (Figs. 4a-d, Supplementary Figs. 28–29). All devices deliver strong and stable EL emission over a wide voltage range of 2.0–7.0 V (Figs. 4e-h). A comprehensive survey of blue perovskite LED EQEs across wavelengths (Figs. 4i-l and Supplementary Table 3) shows that our hetero-TOAF QD-based LEDs outperform all reported devices over the entire blue spectrum, setting record-breaking EQEs for blue perovskite LEDs[19,24,29–45].

Conclusion

In summary, we report a heterogeneous synthesis approach in which undissolved lead halide solids serve as a thermodynamic reservoir, enabling simultaneous control over the growth kinetics and defect landscape of $CsPbBr_xCl_{3-x}$ QDs. This strategy suppresses Cl-vacancy-induced deep-level defects and surface disorder, yielding a quasi-core-shell structure that, together with TOAF passivation, markedly enhances the optoelectronic properties of the QDs. The resulting blue LEDs achieve record EQEs across the full blue spectrum, including a record-breaking EQE of 37.56% at 476 nm. By relaxing the conventional requirement for perfect precursor homogeneity, our work establishes a generalizable design framework for perovskite QD synthesis, showing that deliberate manipulation of precursor phase behavior can fundamentally reshape defect chemistry and device performance. These results thus provide both a mechanistic understanding and a practical pathway for advancing perovskite LEDs toward ultra-high-definition display applications.

Methods

Chemicals

Lead bromide ($PbBr_2$, 99.9%), lead chloride ($PbCl_2$, 99.99%), caesium carbonate (Cs_2CO_3, 99.99%), rubidium carbonate (Rb_2CO_3, 99%), formamidine acetate (FA(Ac), 99%), *n*-octanoic acid (OTAc, 98%), didodecyldimethylammonium chloride (DDAC, 98%), tetra-*n*-octylammonium bromide (TOAB, 98%), dodecylbenzenesulfonic acid (DBSA, 90%), ethyl acetate (EA, 99.5%), chlorobenzene (99.8%), lithium fluoride (LiF, 99.5%), sodium fluoride (NaF, 99.99%), *n*-octane (99%), and toluene (C_7H_8, 90%) were purchased from Aladdin. Nafion perfluorinated ionomer (PFI, 5 wt % in mixture of lower aliphatic alcohols and water, containing 45% water) was purchased from Macklin. 1,3,5-Tris(1-phenyl-1H-benzimidazol-2-yl)benzene (TPBi), 2,4,6-tris[3-(diphenylphosphino)phenyl]-1,3,5-triazole (PO-T2T), poly(ethylenedioxythiophene):poly(styrenesulfonate) (PEDOT:PSS, Heraeus-Clevios PVP AI4083), and poly(9,9-n-diphenyl-2,7-fluorene-alt-9-isophenyl-3,6-carbazole) (PF8Cz) were purchased from Xi'an Yuri Solar Co., Ltd. All chemical reagents were used directly without further purification.

Preparation of Cs-OTAc precursor

Cs-OTAc precursor was prepared by adding Cs_2CO_3 (1.5 mmol), FA(Ac) (0.27 mmol), Rb_2CO_3 (0.15 mmol), and OTAc (18 mL) into a 20 mL vial. The mixture was stirred at room temperature in air until it became clear.

Synthesis of TOAF

TOAF was synthesized according to a previously reported method[46]. TOAB (10 g) and NaF (1.6 g) were dissolved separately in toluene (50 mL) and deionized water (50 mL), respectively. The solutions were transferred to a 500 mL three-necked flask and stirred at room temperature for 3 h. After centrifugation at 6,000 rpm for 5 min, the supernatant was kept at 0°C for 2 h to crystallize. Ethyl acetate (150 mL) was then introduced, and the precipitate was isolated by centrifugation at 12,000 rpm for 10 min, followed by vacuum drying at 60°C for 12 h to yield white crystals.

Synthesis of homo-QDs

$PbCl_2$ (0.1 mmol), $PbBr_2$ (0.4 mmol), DDAC (0.3 mmol), TOAB (0.72 mmol), and toluene (5 mL) were added to a 20 mL vial and stirred at room temperature in air for 4.5 h. DBSA-toluene solution (0.4 mL, 1 g mL^{-1}) was added into the above solution and stirred for 2 min, followed by 0.54 mL Cs-OTAc precursor with stirring for 2 min. Finally, 1.5 mL DDAC-toluene solution (10 mg mL^{-1}) was introduced and stirred for an additional 2 min. Homo-QDs with tunable PL peaks were synthesized by adjusting the precursor ratios, the specific conditions are listed in Supplementary Table 1.

Synthesis of hetero-QDs

$PbCl_2$ (0.15 mmol), $PbBr_2$ (0.4 mmol), DDAC (0.3 mmol), TOAB (0.3 mmol), and toluene (5 mL) were added to a 20 mL vial and stirred at room temperature in air for 4.5 h. DBSA-toluene solution (0.4 mL, 1 g mL^{-1}) was added into the above solution and stirred for 2 min, followed by 0.54 mL Cs-OTAc precursor with stirring for 2 min. Finally, 1.5 mL DDAC-toluene solution (10 mg mL^{-1}) was introduced and stirred for an additional 2 min. Hetero-QDs with tunable PL peaks were synthesized by adjusting the precursor ratios, the specific conditions are listed in Supplementary Table 1.

Synthesis of hetero w/o precipitate QDs

The synthesis procedure was identical to that of hetero-QDs, except that the lead halide precipitate was removed by centrifuging the precursor solution at 4,000 rpm for 3 min before Cs-OTAc injection.

Purification of $CsPbBr_xCl_{3-x}$ QDs

The crude solution was separated by centrifugation at 4,000 rpm for 3 min. Ethyl acetate (14 mL) was added to the supernatant, and the mixture was centrifuged at 9,000 rpm for 3 min. The precipitate was redispersed in 1 mL octane. Ethyl acetate (2 mL) was added to the above solution and centrifuged at 9,000 rpm for 3 min. The precipitate was redispersed in 700 μL octane and centrifuged at 4,000 rpm for

2 min to separate the un-dispersed by-product. The purified QDs were stored at 4°C for 12 h before device fabrication.

TOAF treatment

12 mg of the as-prepared TOAF was added to the purified $CsPbBr_xCl_{3-x}$ QDs. The vial was sealed under nitrogen flow and stirred for 5 h, then kept in the dark at 4°C for 12 h to complete the passivation.

Fabrication of LEDs devices

Patterned ITO-coated glasses were cleaned successively using soap, deionized water, isopropanol, and acetone. Then ITO glasses were subjected to UV-ozone treatment for 30 min. PEDOT:PSS/PFI solution (volume ratio of 1:2) was spin coated onto the ITO substrate at 4000 rpm for 40 s and annealed in air at 150°C for 20 min. The PEDOT:PSS/PFI coated substrates were transferred into an N_2-filled glove box. PF8Cz (5–15 mg/mL) was spin-coated onto the PEDOT:PSS/PFI film at 2000 rpm and annealed at 150°C for 20 min. The perovskite QDs were spin-coated at 8000 rpm for 40 s. TPBi (5 nm), PO-T2T (30 nm), LiF (1.5 nm), and Al (80 nm) layers were sequentially deposited by thermal evaporation in a vacuum deposition chamber (~ 1×10^{-4} Pa).

Electroluminescence characterization of LEDs devices

LEDs with an active area of 4 mm^2 were characterized in a nitrogen-filled glovebox at room temperature. Electroluminescence (EL) spectra were collected using an integrating sphere (50 mm diameter) coupled to a calibrated QE Pro spectrometer (Ocean Optics), with devices mounted at the sphere's entrance aperture to capture emission from the glass side. The devices were driven by a Keithley 2400 source meter at constant current. Absolute EL power spectra were acquired, and the radiance was obtained by integrating the calibrated spectra over 400–760 nm. EQE was calculated from the absolute power spectra and the corresponding current density. For stability tests, the driving current was predetermined using the EQE measurement system. The spectrometer radiance scale was calibrated with a radiometrically calibrated light source (HL-3P-INT-CAL, Ocean Optics). Measurements were repeated on multiple devices to ensure reproducibility.

XPS, UPS, FTIR, and NMR characterization

XPS and UPS were performed on an ESCALAB Xi+ spectrometer (Thermo Scientific) using monochromated Al K_α (1,486.6 eV) and He I (21.2 eV) radiation, respectively. XPS depth profiling was performed on the same instrument using an Ar^+ ion sputtering gun (2,000 eV, ~ 3.5 μA, beam spot ≤ 500 μm, calibrated sputter rate 0.28 nm s^{-1}). The surface was etched layer by layer, and high-resolution XPS spectra were recorded under the same acquisition conditions as for standard XPS. Charge neutralization was achieved using a co-axial dual-beam flood gun to ensure accurate calibration of the C 1s peak position. Spectra were recorded and analysed with Thermo Avantage software. Fourier-transform infrared (FTIR) spectra were acquired on a Nicolet iS50 spectrometer (Thermo Scientific). Colloidal ^{133}Cs NMR spectra were recorded on a Bruker AVANCE III HD 400 MHz spectrometer equipped with a

broadband probe (PROBHD Z108618-0547). The observation frequency for ^{133}Cs was 52.49 MHz. A single-pulse sequence (zg) was used with a 9.0 μs excitation pulse and a 0.5 s recycle delay. Spectra were acquired at 295.6 K with a spectral width of 21,008.4 Hz, 65,536 acquisition points, and 1,700 scans (preceded by 4 dummy scans). Post-processing applied an exponential window function with 20.0 Hz line broadening and a Fourier transform size of 32,768 points.

PL and TRPL spectra measurements

Steady-state PL and TRPL were measured using an Edinburgh Instruments EI-FLS1000 fluorescence spectrometer equipped with an integrating sphere. TRPL decays were recorded with a nanosecond flash lamp (λ_{ex} = 375 nm). Absolute PLQYs were determined using the same spectrometer with a 150 W xenon lamp and a mountable integrating sphere. Temperature-dependent PL was carried out using a Linkam THMS600 stage cooled with liquid nitrogen, the E_b was calculated using an Arrhenius Eq. 4[7].

SEM and TEM measurements

Scanning electron microscopy (SEM) and energy-dispersive X-ray spectroscopy (EDS) were carried out on a Hitachi SU8010 field-emission SEM equipped with an EDAX Octane Elect Super SDD detector, using an accelerating voltage of 10 kV. Transmission electron microscopy (TEM) images were acquired with a Hitachi HT-7700 microscope at 100 kV. High-resolution TEM (HRTEM) and high-angle annular dark-field scanning TEM (HAADF-STEM) images of the QDs were obtained on a JEM-F2000 microscope operated at 200 kV.

TA measurement

Femtosecond transient absorption spectra were recorded on an Ultrafast Systems Helios spectrometer. The laser source was a Coherent Astrella USP Ti:sapphire regenerative amplifier (800 nm, 35 fs, 1 kHz) seeded by a Coherent Vitesse oscillator. The 400 nm pump pulses were produced by an optical parametric amplification system, and the broadband probe pulses were generated by focusing a fraction of the 800 nm fundamental beam into a sapphire crystal.

KPFM and CAFM measurements

The KPFM and CAFM measurements were carried out on an Asylum Research Cypher AFM (Oxford Instruments) equipped with AC, lift and conductive ORCA modes, respectively, using standard silicon and conductive probes.

Transient photocurrent measurements

The transient photocurrent was collected using a Keithley 4200-SCS semiconductor parameter analyzer and monitored under 405 nm laser (ADR-1805) with the same power and a period.

Confocal laser scanning fluorescence microscope

Fluorescence microscopy images were acquired using a Zeiss LSM 980 laser-scanning confocal microscope with a 405 nm diode laser as the excitation source. All images were recorded at room temperature.

Conductivity measurement

Electrical conductivity was evaluated by measuring current-voltage (*I*-*V*) characteristics of ITO/QD/Al capacitor structures using a Keithley 2400 source meter in the dark. Measurements were carried out at room temperature under N_2 atmosphere with a voltage sweep from − 4 to + 4 V (step size 0.1 V). The conductivity (σ) was calculated according to the following formula[42]:

$$\sigma = \frac{Id}{V\mathrm{A}}$$

1

where *d* is the film thickness, A is the effective device area (4 mm^2), *I* and *V* represent the applied voltage and current of the device, respectively.

Ion migration activation energy measurement

The ion migration activation energy (E_a) was determined from temperature-dependent current decay measurements using a Keithley 2400 source meter and a Linkam THMS600 temperature-controlled stage. Unencapsulated QLED devices were placed on the stage inside a N_2-filled glovebox and allowed to equilibrate for 5 min at each temperature. The measurement sequence consisted of a 30 s hold at 0 V, a 50 s step to + 4 V to record the current transient, and a final 30 s at 0 V. At each temperature, the decay portion of the current was fitted with a single-exponential function $I(t) = I_0 + I_1\exp(-t/\tau)$, yielding a decay rate $k = \tau^{-1}$. The E_a is calculated from the temperature-dependent conductance using the Arrhenius relation[28,48,49]:

$$\ln(kT) = C - \frac{E_a}{k_B T}$$

2

where *T* denotes the temperature, *C* is a constant, k_B is the Boltzmann constant.

Declarations

Competing interests

The authors declare that they have no competing interests.

Data and materials availability

All data needed to evaluate the conclusions in the paper are present in the paper or the supplementary materials. Source data are provided with this paper.

Funding

This work was supported by the National Natural Science Foundation of China (NSFC No. 52372159, U25A20235, 12374386), Fundamental Research Funds for the Central Universities of China University of Geosciences (Wuhan) (No. G13235261628), Guangdong Basic and Applied Basic Research Foundation (No. 2023A1515030021, 2024A1515013170), Shenzhen Science and Technology Program (No. JCYJ20220530162405012, 20240813114017022, 20250604183427037), Natural Science Foundation of Wuhan (No. 2024040801020283), Science and Technology Program of Hubei Province (2025EHA058).

Author contributions

K.C conceived the idea. J.C. initialized the project and contributed to the fabrication and characterization of QDs and devices. J.C., W.Z., and X.Z. contributed to device fabrication and characterization. J.C., W.Z., X.Z., Y.W., and Z.P. performed optical properties. F.X., K.C., and G.L. directed and supervised the project. K.C. wrote the manuscript with input from all authors. All authors contributed to discussions and finalizing the manuscript.

Acknowledgments

The authors thank the anonymous reviewers for their constructive comments and suggestions.

References

1. Garcia de Arquer, F. P. *et al.* Semiconductor quantum dots: Technological progress and future challenges. *Science* **373**, eaaz8541 (2021).
2. Alivisatos, A. P. Semiconductor clusters, nanocrystals, and quantum dots. *Science* **271**, 933-937 (1996).
3. Murray, C. B., Norris, D. J. & Bawendi, M. G. Synthesis and characterization of nearly monodisperse CdE (E = sulfur, selenium, tellurium) semiconductor nanocrystallites. *J. Am. Chem. Soc.* **115**, 8706-8715 (1993).
4. Ghosh Chaudhuri, R. & Paria, S. Core/shell nanoparticles: classes, properties, synthesis mechanisms, characterization, and applications. *Chem. Rev.* **112**, 2373-2433 (2011).
5. La Mer, V. K. & Dinegar, R. H. Theory, production and mechanism of formation of monodispersed hydrosols. *J. Am. Chem. Soc.* **72**, 4847–4854 (1950).

6. Hendricks, M. P., Campos, M. P., Cleveland, G. T., Jen-La Plante, I. & Owen, J. S. A tunable library of substituted thiourea precursors to metal sulfide nanocrystals. *Science* **348**, 1226–1230 (2015).
7. Watzky, M. A. & Finke, R. G. Transition metal nanocluster formation kinetic and mechanistic studies. A new mechanism when hydrogen is the reductant: slow, continuous nucleation and fast autocatalytic surface growth. *J. Am. Chem. Soc.* **119**, 10382–10400 (1997).
8. Sosso, G. C. *et al.* Crystal nucleation in liquids: open questions and future challenges in molecular dynamics simulations. *Chem. Rev.* **116**, 7078–7116 (2016).
9. Wu, X.-g., Jing, Y. & Zhong, H. In situ fabricated perovskite quantum dots: from materials to applications. *Adv. Mater.* **37**, 2412276 (2025).
10. Akkerman, Q. A. *et al.* Controlling the nucleation and growth kinetics of lead halide perovskite quantum dots. *Science* **377**, 1406–1412 (2022).
11. Lignos, I. *et al.* Synthesis of cesium lead halide perovskite nanocrystals in a droplet-based microfluidic platform: fast parametric space mapping. *Nano Lett.* **16**, 1869–1877 (2016).
12. Peng, X., Wickham, J. & Alivisatos, A. P. Kinetics of II-VI and III-V colloidal semiconductor nanocrystal growth: "focusing" of size distributions. *J. Am. Chem. Soc.* **120**, 5343–5344 (1998).
13. Chen, Y., Johnson, E. & Peng, X. Formation of monodisperse and shape-controlled MnO nanocrystals in non-injection synthesis: self-focusing via ripening. *J. Am. Chem. Soc.* **129**, 10937–10947 (2007).
14. Zheng, X. *et al.* Chlorine vacancy passivation in mixed halide perovskite quantum dots by organic pseudohalides enables efficient Rec. 2020 blue light-emitting diodes. *ACS Energy Lett.* **5**, 793–798 (2020).
15. Nenon, D. P. *et al.* Design principles for trap-free $CsPbX_3$ nanocrystals: enumerating and eliminating surface halide vacancies with softer Lewis bases. *J. Am. Chem. Soc.* **140**, 17760–17772 (2018).
16. Yuan, S. *et al.* Overcoming degradation pathways to achieve stable blue perovskite light-emitting diodes. *ACS Energy Lett.* **7**, 1348–1354 (2022).
17. Mirabelli, A. J. *et al.* Interfacial chemistry limits the stability of deep blue perovskite LEDs revealed by operando characterization. *ACS Energy Lett.* **10**, 3533–3543 (2025).
18. Xu, Y. *et al.* Multisite cross-linked ligand suppressing ion migration for efficient and stable $CsPbBr_3$ perovskite quantum dot-based light-emitting diodes. *Angew. Chem. Int. Ed.* **64**, e202422823 (2025).
19. Cao, Q. *et al.* Surface-ligand-triggered synthetic control of defects in nanocrystals toward high-efficiency blue electroluminescence. *The Innovation* **7**, 101273 (2026).
20. Allen, L. C. Electronegativity is the average one-electron energy of the valence-shell electrons in ground-state free atoms. *J. Am. Chem. Soc.* **111**, 9003–9014 (1989).
21. Song, J. *et al.* Room-temperature triple-ligand surface engineering synergistically boosts ink stability, recombination dynamics, and charge injection toward EQE-11.6% perovskite QLEDs. *Adv. Mater.* **30**, 1800764 (2018).
22. Yassitepe, E. *et al.* Amine-free synthesis of cesium lead halide perovskite quantum dots for efficient light-emitting diodes. *Adv. Funct. Mater.* **26**, 8757–8763 (2016).

23. Aebli, M. *et al.* Disorder and halide distributions in cesium lead halide nanocrystals as seen by colloidal ^{133}Cs nuclear magnetic resonance spectroscopy. *Chem. Mater.* **36**, 2767–2775 (2024).
24. Nong, Y., Yao, J. & Song, J. Cation-anion-pair-assisted synthesis strategy enables high-performance pure blue perovskite quantum dot-based light-emitting diodes. *Adv. Funct. Mater.* **36**, e20569 (2026).
25. Min, S., Mukherjee, M., Szabó, G., Kamat, P. V. & Cho, J. Design principles of spacer cations for suppressing phase segregation in 2D halide perovskites. *Chem. Sci.* **16**, 21950–21961 (2025).
26. Wang, J. *et al.* Matched electron-transport materials enabling efficient and stable perovskite quantum-dot-based light-emitting diodes. *Angew. Chem. Int. Ed.* **63**, e202410689 (2024).
27. Ren, H. *et al.* 22.8%-EQE and ns-level response $CsPbBr_3$ perovskite quantum dot-based light-emitting diodes. *Adv. Funct. Mater.* **36**, e29207 (2026).
28. Li, H. *et al.* Nanosurface-reconstructed perovskite for highly efficient and stable active-matrix light-emitting diode display. *Nat. Nanotechnol.* **19**, 638–645 (2024).
29. Wang, Y. *et al.* Isomeric multi-hydrogen-bonding enables blue perovskite LEDs. *Nature* **655**, 617–623 (2026).
30. Hong, Y. *et al.* Perovskite nanocrystals protected by hermetically sealing for highly bright and stable deep-blue light-emitting diodes. *Adv. Sci.* **10**, 2302906 (2023).
31. Gao, Y. *et al.* Highly efficient blue light-emitting diodes based on mixed-halide perovskites with reduced chlorine defects. *Sci. Adv.* **10**, eado5645 (2024).
32. Mao, J. *et al.* Interface-regulated vapour crystallization for ultrapure perovskite LEDs. *Nat. Synth.* **5**, 1712–1723 (2026).
33. Li, J. *et al.* Efficient deep-blue (465 nm) perovskite quantum dot-based light-emitting diodes via triphenylamine derivative tailored hole transport engineering. *Adv. Funct. Mater.* **35**, 2412367 (2025).
34. Maimaitizi, H., Ågren, H. & Chen, G. Multifunctional ligand engineering enables high-performance $CsPb(Br/Cl)_3$ nanocrystals toward efficient and stable pure-blue perovskite LEDs. *Light Sci. Appl.* **15**, 135 (2026).
35. Xie, M. *et al.* Ultra-low efficiency roll-off high color purity blue perovskite quantum dot LEDs with exceeding 20% efficiency. *Light Sci. Appl.* **15**, 176 (2026).
36. Kwon, J. *et al.* In situ molecular passivation for improved performance and spectral stability in thermally evaporated pure blue perovskite light-emitting diodes. *Ind. Chem. Mater.* **4**, 355–365 (2026).
37. Chen, H. *et al.* High-quality perovskite crystal for efficient and bright pure-blue light-emitting diodes with narrow emission. *Nat. Commun.* **17**, 4697 (2026).
38. Ma, Z. *et al.* Steric hindrance of ligands inhibits interface ion penetration in perovskite nanocrystal-based electroluminescence devices. *ACS Energy Lett.* **10**, 5754–5761 (2025).
39. Cao, Q. *et al.* Isotropic-grown ultrasmall $CsPbBr_3$ nanocrystals in an enlarged synthesis toward efficient blue electroluminescence. *ACS Nano* **19**, 42455–42465 (2025).

40. Nong, Y. *et al.* The inserted dipole layer enables highly powerful blue perovskite quantum dot-based light-emitting diodes. *Sci. Bull.* **71**, 2758–2766 (2026).
41. Wu, X. *et al.* Ligand-mediated intergrain isolation strategy for narrow-emission deep-blue perovskite quantum dot light-emitting diodes. *ACS Photonics* **13**, 1537–1545 (2026).
42. Nong, Y. *et al.* Boosting external quantum efficiency of blue perovskite QLEDs exceeding 23% by trifluoroacetate passivation and mixed hole transportation design. *Adv. Mater.* **36**, 2402325 (2024).
43. Zhu, M. *et al.* Highly efficient sky-blue perovskite quantum dot light-emitting diodes via ligand-assisted trap-state passivation. *Energy Environ. Mater.* **9**, e70216 (2026).
44. Zheng, S. *et al.* Stable sky-blue perovskite LEDs achieved by efficient sub-bandgap emission with 24.5% PCE. *Adv. Funct. Mater.* **36**, e21079 (2026).
45. Zhang, L. *et al.* Photovoltage-driven two-transistor-one-diode perovskite pixels for in-cell optical sensing displays. *Adv. Mater.* **38**, e22776 (2026).
46. Qin, Z. *et al.* Co-regulation strategy dominated by double short molecules permitting the regrowth of quantum dots for efficient deep-blue perovskite light-emitting diodes. *Nano Energy* **121**, 109263 (2024).
47. Li, M. *et al.* Entropic-ligand-driven efficient and stable $CsPbI_3$ quantum dot light-emitting diodes. *Nano Lett.* **26**, 2651–2659 (2026).
48. Zhang, B.-B. *et al.* Defect proliferation in $CsPbBr_3$ crystal induced by ion migration. *Appl. Phys. Lett.* **116**, 063505 (2020).
49. Peng, C. *et al.* Weakly space-confined all-inorganic perovskites for light-emitting diodes. *Nature***643**, 96–103 (2025).

Figures

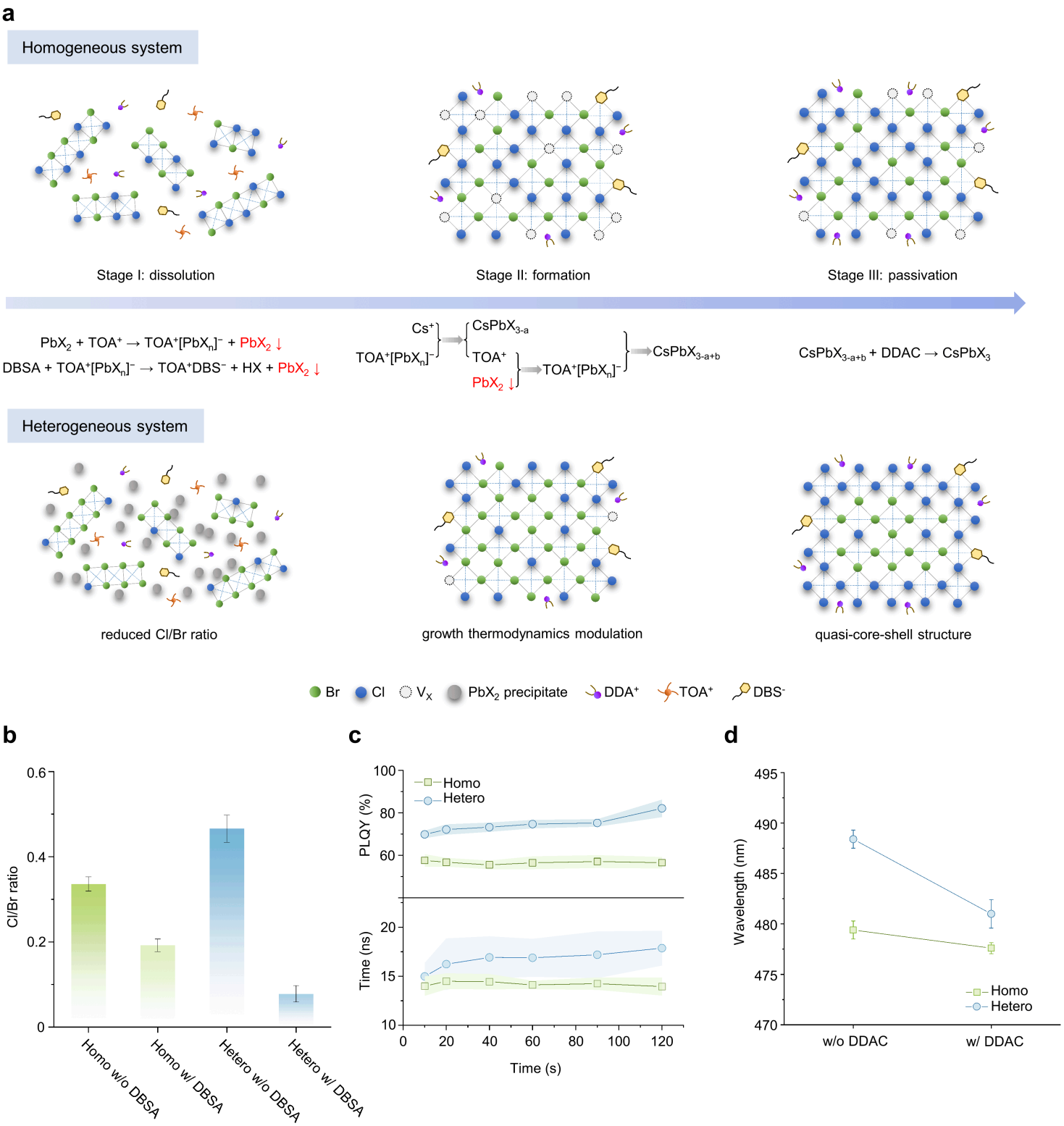


Figure 1

Controlling growth thermodynamics of $CsPbBr_xCl_{3-x}$ QDs. a, Schematic illustrations of the homogeneous (top) and heterogeneous (bottom) synthesis strategies. In the heterogeneous approach, excess PbX_2 and preferential $PbBr_2$ dissolution initially lower the Cl/Br ratio below the feed ratio, an effect further enhanced by DBSA addition. Subsequently, the released TOA^+ ions re-dissolve the solid

PbX_2 precipitate to regenerate $TOA^+[PbX_n]^-$, shifting the equilibrium toward monomer formation and promoting in situ defect passivation. Finally, DDAC treatment passivates residual halide vacancies and yields quasi-core-shell structure with Cl-rich surface. **b**, Comparison of Cl/Br ratios at stage I in the homogeneous and heterogeneous systems. For these measurements, the precursors were centrifuged and the supernatants were deposited on glass substrates. The elemental ratios were determined by SEM-EDS after complete evaporation of volatile species (including less reactive, incompletely ionized HCl and HBr). **c**, Time-dependent PL lifetimes and PLQYs of the QDs following Cs-precursor injection (stage II). **d**, The effect of DDAC on the PL peak wavelengths of the QDs.

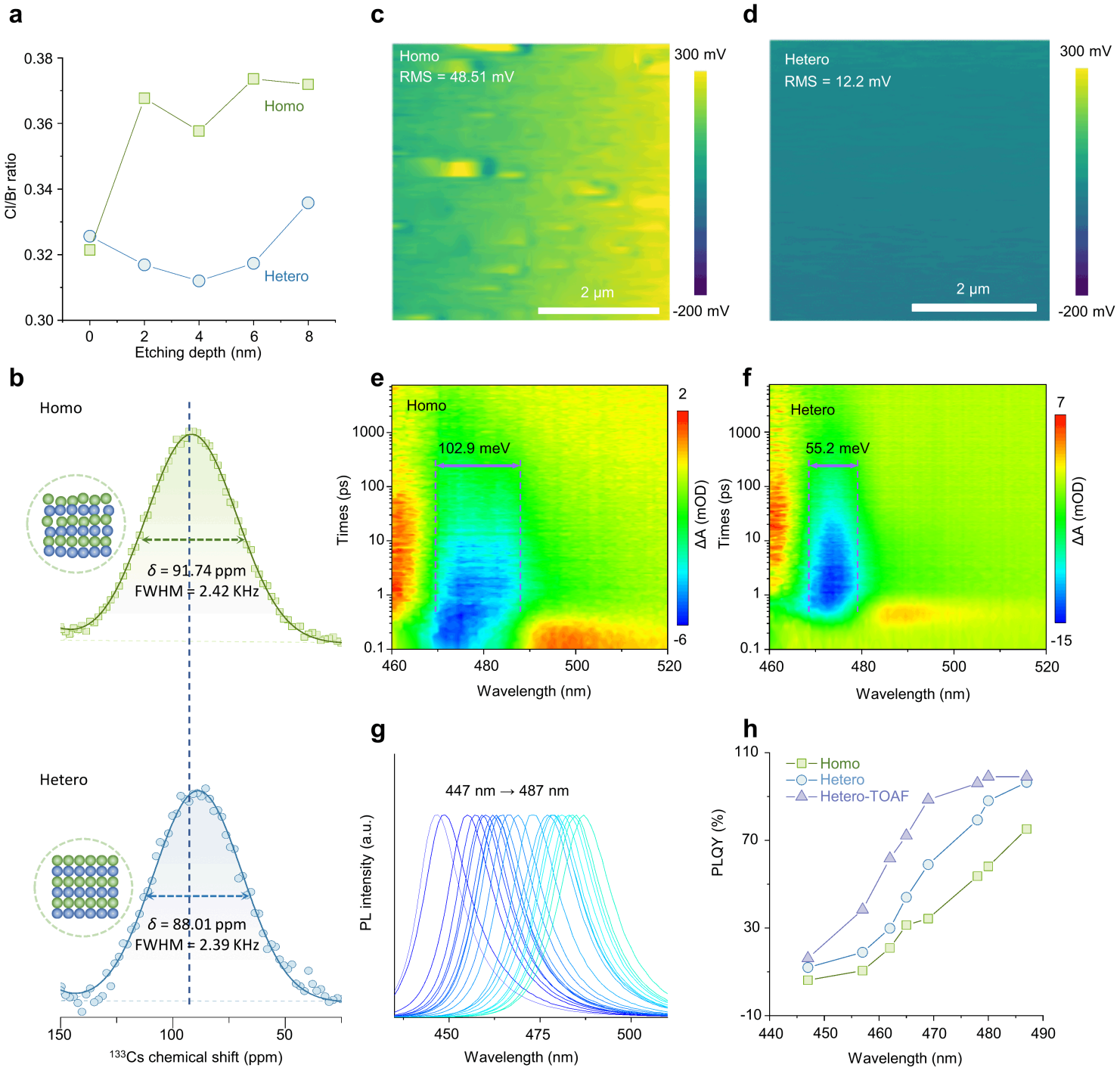


Figure 2

Structural and optical characterization of $CsPbBr_xCl_{3-x}$ QDs. a, Cl/Br ratios as a function of XPS etching depth for homo-QDs and hetero-QDs. **b**, Colloidal ^{133}Cs NMR spectra of homo-QDs (top) and hetero-QDs (bottom). Inserts demonstrate the disordered and ordered surface. **c,d**, KPFM images of homo-QD (**c**) and hetero-QD (**d**) films. **e,f**, Pseudo-colour TA spectra and pump-detection delay time for homo-QD (**e**) and hetero-QD (**f**) films. **g,h**, PL spectra (**g**) and PLQY values (**h**) of QDs with systematically tuned Cl/Br stoichiometry.

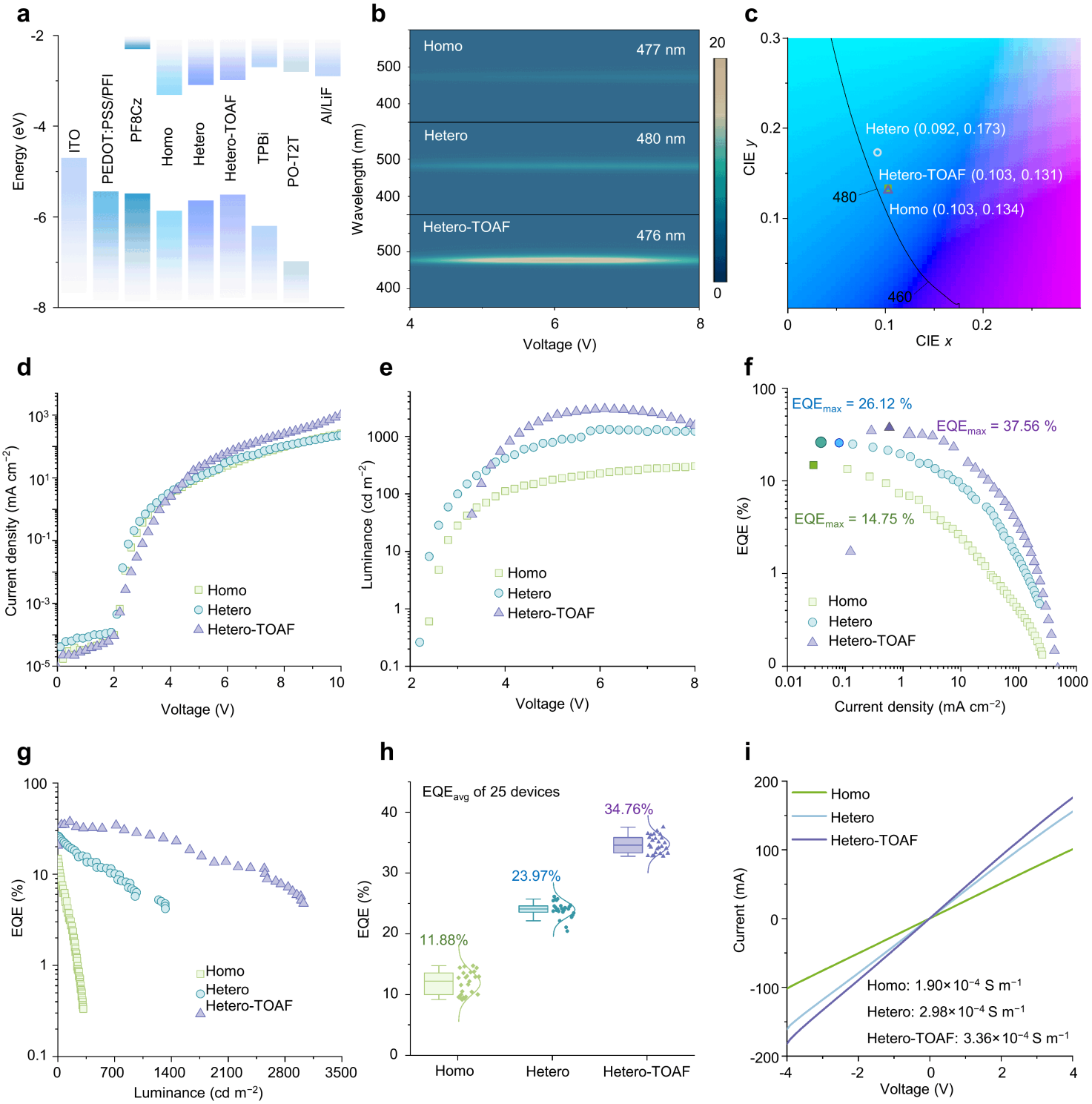


Figure 3

Electroluminescence performance of $CsPbBr_xCl_{3-x}$ QD-based LEDs. a, Schematic energy band diagram of the LED structure. **b,c**, Electroluminescence spectra at increasing driving voltages (**b**) and the corresponding chromaticity coordinates on the CIE 1931 diagram (**c**) for homo-, hetero-, and hetero-TOAF QD devices. **d**, Current density-voltage curves. **e**, Luminance-voltage curves. **f**, EQE as a function of current density. **g**, EQE as a function of luminance. **h**, Statistical distribution of peak EQEs from 25 devices for each LED type. **i**, Current-voltage characteristics of ITO/QDs/Al capacitor structures.

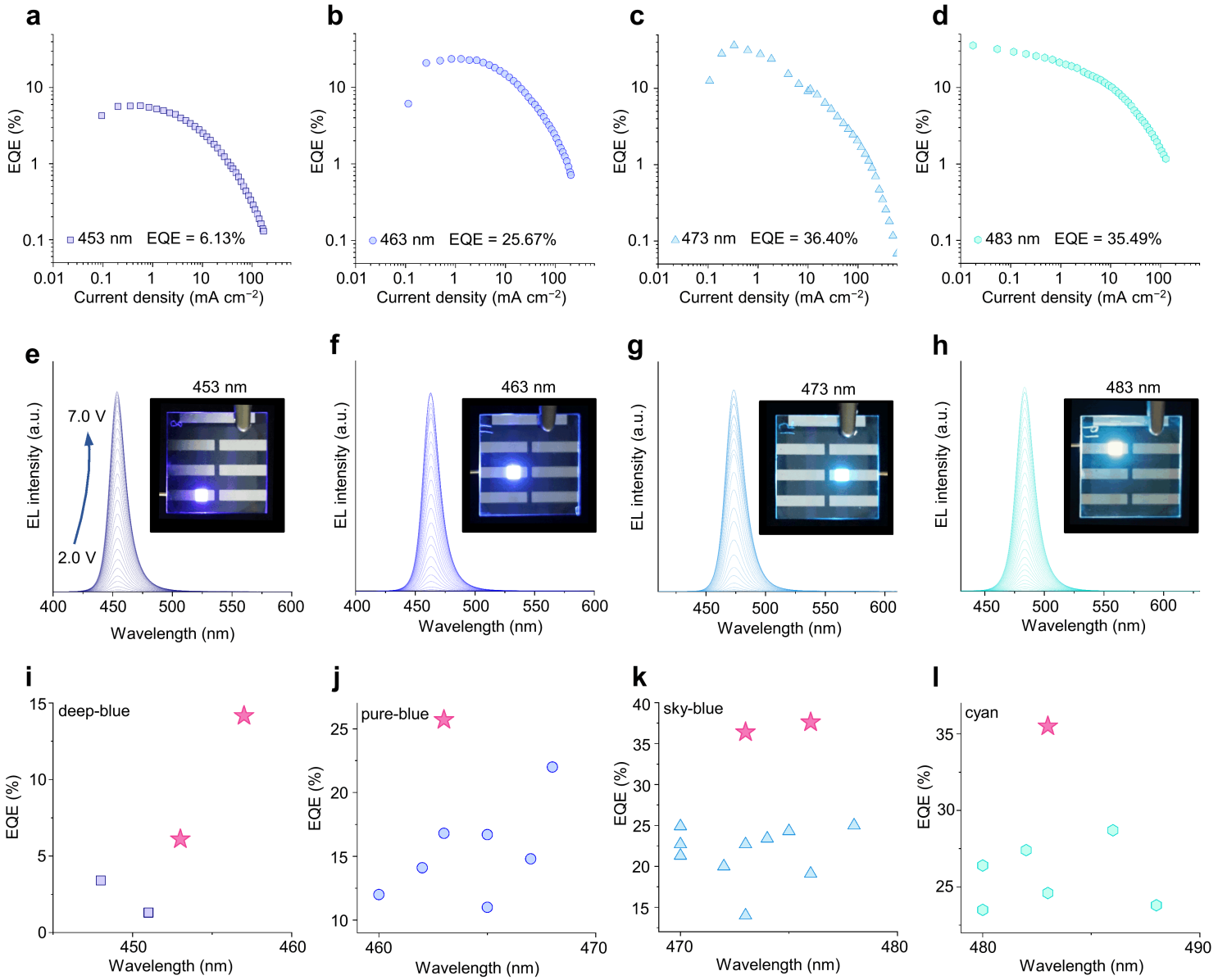


Figure 4

Electroluminescence performance of blue LEDs with different emission wavelengths. a-d, EQE-current density curves of devices with peak emission at 453 nm (**a**), 463 nm (**b**), 473 nm (**c**), and 483 nm (**d**). **d-g**, Voltage-dependent electroluminescence spectra of devices with peak emission at 453 nm (**d**), 463 nm (**e**), 473 nm (**f**), and 483 nm (**g**). Insets: corresponding optical photographs of the operating devices. **h-k**,

Comparison of our peak EQE values (denoted as stars) with previously reported values for deep-blue (**h**), pure-blue (**i**), sky-blue (**j**), and cyan (**k**) perovskite LEDs.

Supplementary Files

This is a list of supplementary files associated with this preprint. Click to download.

- SupplementaryInformation.pdf